# Innovative thermal management for liquid hydrogen aero engines: a comparison with kerosene systems

*Weitong Liu[1,2], Xiuting Gu[1,2], Yiang Liu[1,2], Jiayang Wang[1,2], Ruoyu Wang[1,2], Yanchen Fu[1,2,†]*
*1 Research Institute of Aero-engine, Beihang University, Beijing 100191, China*
*2 Collaborative Innovation Center for Advanced Aero-Engine, Beihang University, Beijing 100191, China*
First Author e-mail: 17375161@buaa.edu.cn
[†] Corresponding Author, yanchenfu@buaa.edu.cn

## Abstract
This paper presents a novel hydrogen-fueled turbofan engine featuring a TMS based on an indirect cooling cycle. A thermodynamic model is developed using the heat current method, and its accuracy is verified through comparison with existing engine data. Compared to kerosene, hydrogen improves heat exchange rates by up to 10.63 times and reduces turbine inlet temperature by 196.9 K. At cruise, it achieves 98.95 kN thrust, 0.60 thermal efficiency, and 0.36 propulsive efficiency. Specific fuel consumption is reduced to 0.33–0.40 times that of kerosene, confirming hydrogen's energy efficiency and its strong potential for decarbonized aviation.

## 1. Introduction

Anthropogenic climate change is significantly impacted by aviation, contributing 12% of global greenhouse gas emissions and emphasizing the urgent need for sustainable aviation solutions [1]. According to projections from the International Civil Aviation Organization's environmental protection panel, global aviation-related $CO_2$ emissions are expected to rise by approximately 21% by 2040 compared to 2015 levels [2]. Hydrogen, as a promising alternative to fossil fuels, has emerged as a revolutionary option for future aviation. However, hydrogen-fueled aero engines face several thermal management challenges: i) Preheating of liquid hydrogen (LH2). Stored onboard in liquid form, LH2 has an extremely low boiling point (20.37 K at 1 atm). It must be regasified before entering the combustor, a process achieved by absorbing heat through a series of heat exchangers. ii) Safety risks of hydrogen heat exchange. Direct heat exchange between hydrogen and high-temperature air poses a fire risk if the heat exchange elements fail. iii) Efficient utilization of $LH_2$ heat sink. Maximizing the high-quality cold source of LH2 for multi-level utilization of the engine's thermal energy is essential for enhancing its thermal efficiency and performance. Therefore, developing advanced thermal management systems (TMS) for hydrogen-fueled aero engines is crucial.

A reliable TMS plays a vital role in maintaining hydrogen's safety and operational effectiveness across varying flight conditions, and directly affects aero-engine performance and economic feasibility. Several studies have explored the utilization of $LH_2$'s cryogenic energy to improve engine efficiency. Techniques include using $LH_2$ to cool compressed air [3], ram air [4], turbine cooling air [5], lubricating oil, and even exhaust gases [6]. In recent developments, the ENABLEH2 project in Europe employed a multi heat exchanger (HEX) TMS to achieve precooling, intercooling, and heat regeneration, thus enhancing engine efficiency while lowering combustor temperatures [7]. Similarly, Pratt & Whitney introduced the HySIITE concept [8], where steam is generated via heat exchange between $LH_2$ and exhaust gas, with the steam later reheated and injected to reduce $NO_x$ emissions and flame temperature. Nevertheless, these configurations often involve direct heat exchange between cryogenic hydrogen and hot gases, which may incur significant exergy losses due to the large temperature gradient. The FlyZero project, led by ATI and backed by the UK government, identified opportunities for exhaust heat recovery integration by 2026 [9], but also faced challenges related to heat transfer losses in extreme temperature differences. To address this, advanced concepts have emerged. For instance, intercooled-recuperated engine architectures showed improved fuel efficiency during takeoff [10]. Other studies proposed incorporating intermediate heat exchange cycles, such as helium loops, enabling the simultaneous utilization of $LH_2$ cold energy and turbine exhaust heat [4].

Achieving safe and effective thermal exchange is essential for hydrogen-powered aero engines. However, hydrogen's inherent flammability presents major safety challenges. HEXs in aero engines typically operate under varying load conditions [11], which can lead to structural vulnerabilities. If HEXs fail during direct contact between $LH_2$ and hot air, the resulting risk of ignition or explosion becomes significant. To mitigate these concerns, researchers have advanced the concept of an intermediate-cycle heat transfer system. This approach introduces a stable working fluid that acts as a thermal bridge, allowing heat to be indirectly exchanged between fuel and high-temperature air through two separate HEXs positioned within the intermediate loop [12, 13]. Liu et al. [14] introduced a multi-fluid, multi-stage heat exchange configuration capable of performing fuel preheating alongside the cooling of bearing chamber air and compressor bleed air. Their combined experimental validation and theoretical analysis demonstrated that the deviation between predicted and actual thermodynamic parameters remained within 10% [15]. Cheng et al. [16] proposed an indirect fuel-cooled thermal management strategy tailored for hydrocarbon-fueled scramjets. This system employs liquid metal as the intermediate heat transfer medium, and its thermal behavior was evaluated in terms of cooling effectiveness and system performance. Overall, the intermediate cycle heat exchange (ICHE) system offers multiple advantages and has played an increasingly important role in the thermal management of aircraft engines. This is particularly true for hydrogen-fueled turbofan engines, where the system enables $LH_2$ preheating, enhances the cascade utilization of energy, and contributes to improved operational safety.

Replacing conventional aviation kerosene with hydrogen leads to substantial changes in the thermodynamic behavior, cost structure, and sustainability profile of propulsion systems—a topic that continues to draw considerable academic interest. Balli et al. [17] conducted a thermodynamic comparison of the TF33 turbofan engine fueled by hydrogen versus kerosene, reporting significant reductions in specific fuel consumption and fuel mass flow by 60.61% and 63.83%, respectively. However, this came with a moderate decline in thrust and a sharp increase in fuel cost rate, rising by nearly 291%. Similarly, Oğur et al. [1, 18] examined the GEnx-1B76 engine at varying altitudes and found that hydrogen provided greater takeoff thrust but less cruise performance, due to reduced fuel mass flow. Despite elevated operational costs, hydrogen was considered a greener alternative. Studies on the GE90 engine by Derakhshandeh et al. [19] echoed these findings, reinforcing the trade-offs between efficiency and sustainability in hydrogen-based propulsion. Further analysis by Akdeniz and Balli [20] on the PW4056 high-bypass turbofan revealed a drop in overall exergy efficiency from 26.9% (kerosene) to 24.3% (hydrogen). In both fuel scenarios, the combustor remained the least efficient component, with hydrogen operation reducing its exergy efficiency to 58.20%, compared to 64.24% for kerosene.

A highly efficient modeling method is essential for directly understanding and analyzing the thermodynamic characteristics of the hydrogen-fueled aero engine. Present modeling techniques are based on stacking governing equations according to component layout to develop the mathematical model of the engine, facing issues such as poor convergence stability, long computational times, and low simulation accuracy [21]. Chen et al. [22] applied the radiation-network approach and thermo-electrical analogy to redefine the thermal resistance of heat exchangers using inlet temperature differences, which led to the formulation of the heat current method [23]. This technique leverages the energy flow topology of thermal systems, which minimizes reliance on auxiliary variables. Given the complex coupling of multiple parameters for hydrogen engines, the heat current method offers a promising alternative for thermodynamic modeling in hydrogen turbofan applications.

This study proposes a novel hydrogen-fueled turbofan engine equipped with a TMS based on an indirect cooling cycle. The system integrates four HEXs and a closed-loop helium cycle to achieve multiple thermal functions, including $LH_2$ preheating, intercooling, recuperation, and compressor bleed air cooling. Leveraging the thermo-electricity analogy, the energy flow model of the hydrogen-fueled turbofan engine was developed using the heat current method. Finally, a comparative analysis was conducted on the thermodynamic performance of the proposed engine fueled with $LH_2$ and kerosene under identical operating conditions.

## 2. System description

Turbofan engines, a subtype of gas turbine engines, comprise several key components: a fan (FAN), a fan nozzle (FDN), low- and high-pressure compressors (LPT and HPT), a combustion chamber (CC), high - and low-pressure turbines (HPT and LPT), and an exhaust nozzle (EDN). Figure 1 illustrates the structure of the proposed thermal management layout for hydrogen-fueled turbofan engines, which integrates a conventional separate-flow turbofan, an intermediate-cycle loop, and a recuperator (HEX-4). This design serves three main purposes: preheating cryogenic $LH_2$ prior to combustion, dissipating onboard heat loads, and recovering exhaust heat to support efficient multi-level energy utilization. To ensure thermal stability and system safety, helium (He) is selected as the intermediate fluid due to its chemical inertness, excellent thermal conductivity, and reliable performance at cryogenic temperatures. The system comprises four counterflow-type heat exchangers:

- **HEX-1** cools the air before it enters the high-pressure compressor, thereby reducing thermal loads and compressor power consumption.
- **HEX-2** functions as a cooled cooling air (CCA) unit, using helium to improve turbine cooling air quality, which allows a higher turbine inlet temperature.
- **HEX-3** facilitates full vaporization and preheating of $LH_2$ to combustion-ready temperatures.
- **HEX-4** raises the air inlet temperature to the combustion chamber by recovering heat from the low-pressure turbine exhaust, thus reducing specific fuel consumption (*SFC*). The intercooler also boosts the temperature gradient across the recuperator, improving waste heat recovery efficiency.

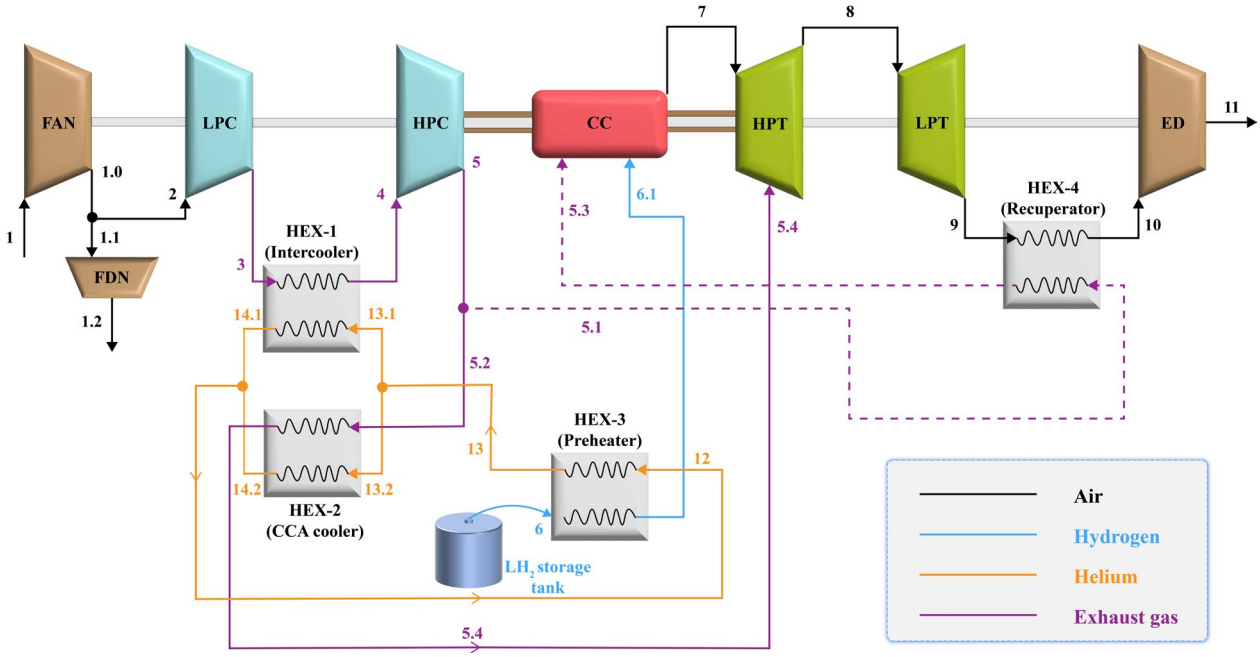


Figure 1: Simplified schematic view of the proposed hydrogen-fueled turbofan engine.

Cryogenic $LH_2$ acts as the terminal heat sink, cooling both compressed air and exhaust gases. Drawing from the design features of the F119 and TF33 engines, key performance parameters are adapted to define a hydrogen turbofan operating at sea-level takeoff conditions, with detailed specifications provided in Table 1.

Table 1: The proposed engine specifications at sea-level takeoff conditions.

| Parameter | Value | Parameter | Value |
|---|---|---|---|
| Air mass flow rate | 150 kg/s | Turbine isentropic efficiency ($\eta_{T,s}$) | 0.93 |
| Helium mass flow rate ($m_{12}$) | 0.8 kg/s | Combustion efficiency ($\eta_{CC}$) | 0.99 |
| Distribution ratio of helium flow in branches ($\phi$) | 0.8 | CC pressure recovery factor ($\sigma_{CC}$) | 0.94 |
| Helium pressure ($P_{12}$) | 3 MPa | HEX pressure recovery factor ($\sigma_{HEX}$) | 0.95 |
| Bypass ratio ($B$) | 1.2 | Mechanical efficiency ($\eta_m$) | 0.99 |
| Pressure ratio of FAN ($\pi_{FAN}$) | 1.77 | Compressor bleed air ratio ($\delta_{HPC}$) | 0.1 |
| Pressure ratio of LPC ($\pi_{LPC}$) | 2.42 | $KA_1$ | 6 kW/K |
| Pressure ratio of HPC ($\pi_{HPC}$) | 5.8 | $KA_2$ | 2 kW/K |
| Fan isentropic efficiency ($\eta_{FAN,s}$) | 0.93 | $KA_3$ | 10 kW/K |
| Compressor isentropic efficiency ($\eta_{C,s}$) | 0.91 | $KA_4$ | 3 kW/K |

## 3. Thermodynamic modeling based on the heat current method

A highly efficient modeling method is essential for directly understanding and analyzing the thermodynamic characteristics of the aero engine. The proposed hydrogen-fueled engines have a more complex structure than the

traditional engine, with a problem of multiple parameters coupling, which poses higher challenges such as poor convergence stability, long computational times, and low simulation accuracy. Based on the thermo-electricity analogy, the energy flow model for the hydrogen-fueled turbofan engine was developed in this paper via the heat current method [23]. The thermodynamic modeling of gas turbine engines in this study is carried out under the following assumptions:

(1) All components operate under steady-state conditions.

(2) Both air and combustion products are considered ideal gases, and complete combustion is assumed.

(3) The system is considered to be adiabatic except for HEXs.

(4) With the exception of HEX-3, the thermophysical properties of the working fluids are determined using their average pressure and temperature.

(5) $LH_2$ flowing from the storage tank is assumed to be saturated, with its saturation temperature defined by its corresponding pressure.

### 3.1 Heat current model of the engine

For the counter-flow type HEX, the inlet temperature-based thermal resistance $R$ is

$$R = \frac{T_{\mathrm{h,in}} - T_{\mathrm{c,in}}}{Q} = \frac{G_{\mathrm{c}} \exp\left(\frac{KA}{G_{\mathrm{h}}}\right) - G_{\mathrm{h}} \exp\left(\frac{KA}{G_{\mathrm{c}}}\right)}{G_{\mathrm{h}} G_{\mathrm{c}} \left[\exp\left(\frac{KA}{G_{\mathrm{h}}}\right) - \exp\left(\frac{KA}{G_{\mathrm{c}}}\right)\right]} \tag{1}$$

where $Q$ is the heat transfer rate, $T$ is the temperature, $KA$ is the thermal conductance of HEX, i.e., the product of heat transfer coefficient and heat transfer area, $G$ is the fluid heat capacity flow rate, i.e., the product of mass flow rate ($m$) and isobaric specific heat capacity ($c_p$). The subscripts $c$ and $h$ represent the cold and hot side fluids of the HEX, respectively.

Employing the heat current method, it is possible to construct the energy flow model of the hydrogen-fueled turbofan engines by connecting state points with the same temperature, as depicted in Figure 2.

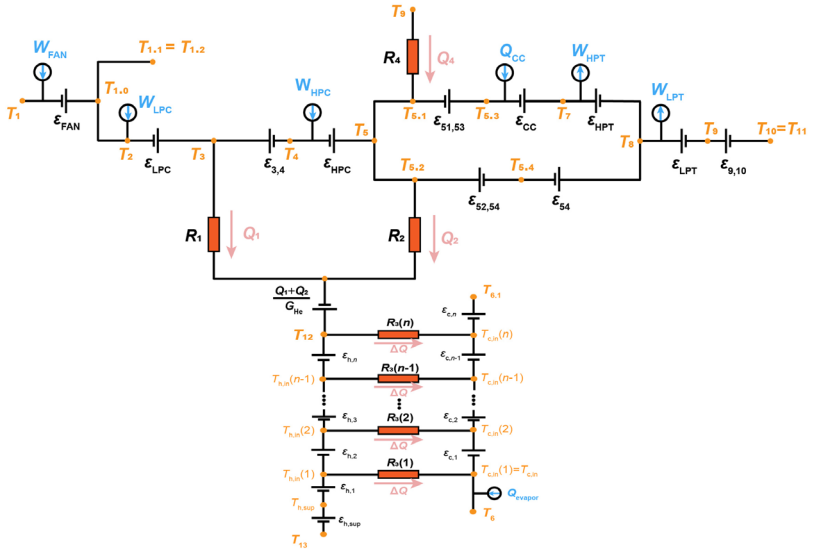


Figure 2: Heat current model of the engine.

As depicted in Figure 2, the heat current model of the engine incorporates a thermal-motive force, $\varepsilon$, which reflects temperature variations of the working fluid resulting from heat transfer, compression, combustion, and expansion processes. $Q_{\mathrm{CC}}$ represents the thermal energy released during fuel combustion. In the fan and compressor stages, air

undergoes compression and gains energy, whereas in the turbine stage, expanding gases deliver work and release energy. Therefore, work terms, $W_i$, are introduced to represent energy inputs and outputs within these components. Each HEX is characterized by its heat transfer rate $Q_i$, and corresponding thermal resistance, $R_i$. In particular, in the fuel preheater HEX-3, heat absorption results in a temperature rise and substantial changes in thermophysical properties. To ensure the applicability of the thermal resistance definition in Eq. (1), a segmentation approach is employed, wherein HEX-3 is equivalently represented by $n$ serially connected HEXs. In the course of thermodynamic analysis, the thermophysical properties of all working fluids are obtained using the open-source property database CoolProp [24]. The system's topological relations can be expressed through mathematical equations derived from Kirchhoff's voltage law (KVL) in the following section.

### 3.2 Modeling of hydrogen-fueled aero engine components

**Environment and Intake**

The standard atmospheric model is adopted for the inlet. The flight altitude $H$ and flight Mach number $Ma$ are input. Firstly, the atmospheric temperature ($T_0$) and pressure ($P_0$) are calculated through the altitude:

$$T_0 = \begin{cases} 288.15 - 0.0065H & H \le 11000\text{m} \\ 216.7 & H > 11000\text{m} \end{cases} \tag{2}$$

$$P_0 = \begin{cases} 101325 \times \left(1 - \dfrac{H}{44308}\right)^{5.2553} & H \le 11000\text{m} \\ 22700 e^{\frac{11 - H/1000}{6.338}} & H > 11000\text{m} \end{cases} \tag{3}$$

For a given $Ma$, the total temperature ($T_1$) and total pressure ($P_1$) at the inlet are determined accordingly.

$$\begin{cases} T_1 = T_0 \left(1 + \dfrac{k-1}{2} Ma^2\right) \\ P_1 = P_0 \left(1 + \dfrac{k-1}{2} Ma^2\right)^{\frac{k}{k-1}} \end{cases} \tag{4}$$

where $k$ is the specific heat ratio with a value of 1.4 for air.

## FAN and FDN

FAN serves as a compressing component. The compressed air exiting the FAN is divided between the engine core and the bypass duct, with the bypass stream ultimately exiting through the FDN. The relationship between input and output parameters is listed below:

$$\begin{cases} \varepsilon_{\text{FAN}} = T_{1.0} - T_1 = T_1 \left( \pi_{\text{FAN}}^{\frac{k-1}{k}} - 1 \right) / \eta_{\text{FAN,s}} \\ W_{\text{FAN}} = G_1 \left( T_{1.0} - T_1 \right) \\ P_{1.0} = \pi_{\text{FAN}} P_1 \\ m_{1.2} = m_{1.1} = m_{1.0} \dfrac{B}{1+B} \\ T_{1.2} = T_{1.1} = T_2 = T_{1.0} \\ P_{1.2} = P_{1.1} = P_2 = P_{1.0} \end{cases} \tag{5}$$

## LPC and HPC

LPC and HPC are also compression components. The calculation process of LPC and HPC is similar to the FAN:

$$\begin{cases} m_3 = m_2 = \dfrac{m_{1.0}}{B+1} \\ \varepsilon_{\mathrm{LPC}} = T_3 - T_2 = T_2\left(\pi_{\mathrm{LPC}}^{\frac{k-1}{k}} - 1\right) / \eta_{\mathrm{C,s}} \\ W_{\mathrm{LPC}} = G_2\left(T_3 - T_2\right) \\ P_3 = \pi_{\mathrm{LPC}} P_2 \\ \varepsilon_{\mathrm{HPC}} = T_5 - T_4 = T_4\left(\pi_{\mathrm{HPC}}^{\frac{k-1}{k}} - 1\right) / \eta_{\mathrm{C,s}} \\ W_{\mathrm{HPC}} = G_4\left(T_5 - T_4\right) \\ P_5 = \pi_{\mathrm{HPC}} P_4 \end{cases} \tag{6}$$

## CC

The air required for combustion is supplied from the outlet of the HPC. Before entering the CC, this airflow passes through HEX-4, where it recovers waste heat from the turbine exhaust. Considering that a portion of the HPC's bleed air is diverted for turbine cooling, the effective mass flow rate of air participating in combustion is determined by the Eq. (7).

$$m_{5.3} = m_5\left(1 - \delta_{\mathrm{HPC}}\right) \tag{7}$$

Given the fuel lower heating value (*LHV*), the thermodynamic parameters at CC can be calculated by:

$$\begin{cases} m_7 = m_{5.3} + m_{6.1} \\ \varepsilon_{\mathrm{CC}} = T_7 - T_{5.3} = \dfrac{m_{6.1} LHV \eta_{CC} + m_{5.3} c_{p,5.3} T_{5.3}}{m_7 c_{p,7}} - T_{5.3} \\ P_7 = P_{5.3} \sigma_{CC} \end{cases} \tag{8}$$

**HPT and LPT**

Both HPT and LPT can be classified as expanding components, and the governing equations are given by:

$$\begin{cases} m_8 = m_7 + m_{5.4} \\ \varepsilon_{\mathrm{HPT}} = T_7 - T_8 = W_{\mathrm{gas}} / G_7 \\ \varepsilon_{54} = T_8 - T_{5.4} = W_{\mathrm{CA}} / G_{5.4} \\ W_{\mathrm{HPT}} = W_{\mathrm{gas}} + W_{\mathrm{CA}} \\ W_{\mathrm{HPC}} = W_{\mathrm{HPT}} \eta_{\mathrm{m}} \\ P_8 = P_7\left[1 - \left(1 - \dfrac{T_8}{T_7}\right) / \eta_{\mathrm{T,s}}\right]^{\frac{k_{g,\mathrm{HPT}}}{k_{g,\mathrm{HPT}}-1}} \end{cases} \tag{9}$$

$$\begin{cases} \varepsilon_{\mathrm{LPT}} = T_8 - T_9 = W_{\mathrm{LPT}} / G_8 \\ W_{\mathrm{FAN}} + W_{\mathrm{LPC}} = W_{\mathrm{LPT}} \eta_{\mathrm{m}} \\ P_9 = P_8\left[1 - \left(1 - \dfrac{T_9}{T_8}\right) / \eta_{\mathrm{T,s}}\right]^{\frac{k_{g,\mathrm{LPT}}}{k_{g,\mathrm{LPT}}-1}} \end{cases} \tag{10}$$

where $W_{\mathrm{CA}}$ and $W_{\mathrm{gas}}$ represent the work done by the turbine cooling air and the exhaust gas, respectively.

**EDN**

Given that the expansion ratio of the EDN is relatively small, its effect is considered negligible. As a result, the inlet and outlet parameters are assumed to follow the expression below:

$$\begin{cases} m_{11} = m_{10} \\ T_{11} = T_{10} \\ P_{11} = P_{10} \end{cases} \tag{11}$$

**Heat exchange process**

The heat exchange components within the engine include the ICHE system and HEX-4, where the ICHE system consists of HEX-1, HEX-2, and HEX-3. Based on Figure 2 and the KVL, the constraint equations for each component can be derived. For HEX-4, the following condition is satisfied:

$$\begin{cases} T_{5.1} = T_{5.2} = T_5 \\ T_9 - T_{5.1} = Q_4 R_4 \\ \varepsilon_{51,53} = T_{5.3} - T_{5.1} = Q_4 / G_{5.1} \\ \varepsilon_{9,10} = T_9 - T_{10} = Q_4 / G_9 \\ P_{10} = P_9 \sigma_{\mathrm{HEX}} \end{cases} \tag{12}$$

ICHE system:

$$\begin{cases} \phi = m_{13.1} / m_{12} = 1 - m_{13.2} / m_{12} \\ T_3 - T_4 = Q_1 / G_3 \\ T_3 - T_{12} = Q_1 R_1 - \left(Q_1 + Q_2\right) / G_{\mathrm{He}} \\ T_{5.2} - T_{12} = Q_2 R_2 - \left(Q_1 + Q_2\right) / G_{\mathrm{He}} \\ T_{5.2} - T_{5.4} = Q_2 / G_{5.2} \\ Q_3 = Q_1 + Q_2 \\ P_4 = P_3 \sigma_{\mathrm{HEX}} \\ P_{5.4} = P_{5.2} \sigma_{\mathrm{HEX}} = P_5 \sigma_{\mathrm{HEX}} \end{cases} \tag{13}$$

$$\begin{cases} Q_{\mathrm{evapor}} = m_{\mathrm{hydrogen}} L_{\mathrm{v}} \\ Q_3 = Q_{\mathrm{sup}} + Q_{\mathrm{evapor}} \\ n = Q_{\mathrm{sup}} / \Delta Q \\ R_3\left(i\right) = \dfrac{G_{\mathrm{H_2}}\left(i\right) \exp\left(\dfrac{KA_3}{G_{\mathrm{He}}}\right) - G_{\mathrm{He}} \exp\left(\dfrac{KA_3}{G_{\mathrm{H_2}}\left(i\right)}\right)}{G_{\mathrm{H_2}}\left(i\right) G_{\mathrm{He}} \left[\exp\left(\dfrac{KA_3}{G_{\mathrm{He}}}\right) - \exp\left(\dfrac{KA_3}{G_{\mathrm{H_2}}\left(i\right)}\right)\right]} \\ T_{\mathrm{h,in}}\left(i\right) = T_{\mathrm{c,in}}\left(i\right) + \Delta Q R_3\left(i\right) \\ T_{\mathrm{c,out}}\left(i\right) = T_{\mathrm{c,in}}\left(i\right) + \Delta Q / G_{\mathrm{H_2}}\left(i\right) \\ T_{\mathrm{h,out}}\left(i\right) = T_{\mathrm{h,in}}\left(i\right) - \Delta Q / G_{\mathrm{He}} \end{cases} \tag{14}$$

Here, $\phi$ denotes the helium flow distribution ratio across branches. $Q_{\mathrm{evapor}}$ represents the heat absorbed during $LH_2$ evaporation, where $L_{\mathrm{v}}$ is the latent heat of vaporization. $Q_{\mathrm{sup}}$ refers to the heat transferred within the superheating zone. The heat transfer in each discrete segment is denoted as $\Delta Q$ and is uniformly set to 1 kW. The HEX-3 is divided into $n$ segments, with $i$ indicating the $i$-th segment.

### 3.3 Model validation

Based on the engine model established in Section 3.2, by inputting the engine parameters listed in Table 1, the thermodynamic parameters at each component node can be solved using an iterative algorithm. During the comparative analysis with different fuels, the inlet pressure of hydrogen fuel is set to 0.5 MPa [25], while that of aviation kerosene is set to 3 MPa [26]. Based on the resolved thermodynamic parameters of each component within the engine, key performance indicators—including engine thermal performance, thrust output, and economic efficiency—can be systematically evaluated between hydrogen fuel and aviation kerosene.

To validate the proposed heat current model for hydrogen-fueled engines, the modeling approach developed in this work is applied to recalculate the thermodynamic parameters of the hydrogen-adapted TF33 turbofan engine, as reported in Ref. [17].

Table 2 presents a comparison between the simulation results of this study and those reported in Ref. [17], where station numbering follows the referenced definitions. The largest temperature deviation appears at the LPT outlet, reaching 3.11%, while the maximum pressure deviation is –10.72% at the HPT outlet. Upstream of the CC outlet, all deviations remain below 1%. Figure 3 further shows the error distribution across all evaluated data points.

Table 2: The comparison between the simulation results and those reported in the reference.

| Station No. | Fluid type | Ref. $T$ (K) | Cal. $T$ (K) | Error of $T$ (%) | Ref. $P$ (K) | Cal. $P$ (K) | Error of $P$ (%) |
|---|---|---|---|---|---|---|---|
| 1 | Air | 288.15 | 288.15 | 0.00 | 101.33 | 101.33 | 0.00 |
| 2 | Air | 350.40 | 350.32 | 0.02 | 179.21 | 179.20 | 0.01 |
| 3 | Air | 350.40 | 350.32 | 0.02 | 179.21 | 179.20 | 0.01 |
| 4 | Air | 348.65 | 350.32 | -0.48 | 177.42 | 179.20 | -1.00 |
| 5 | Air | 350.40 | 350.32 | 0.02 | 179.21 | 179.20 | 0.01 |
| 6 | Air | 461.37 | 461.09 | 0.06 | 434.25 | 434.23 | 0.00 |
| 7 | Air | 652.60 | 652.90 | -0.05 | 1378.57 | 1378.50 | 0.01 |
| 8 | Fuel | 298.15 | 298.15 | 0.00 | 220.60 | 220.60 | 0.00 |
| 9 | Exhaust gas | 1098.42 | 1108.77 | -0.94 | 1309.60 | 1309.57 | 0.00 |
| 10 | Exhaust gas | 942.82 | 944.01 | -0.13 | 510.50 | 565.25 | -10.72 |
| 11 | Exhaust gas | 743.23 | 720.08 | 3.11 | 135.45 | 140.04 | -3.39 |
| 12 | Exhaust gas | 740.07 | 720.08 | 2.70 | 133.25 | 140.04 | -5.10 |

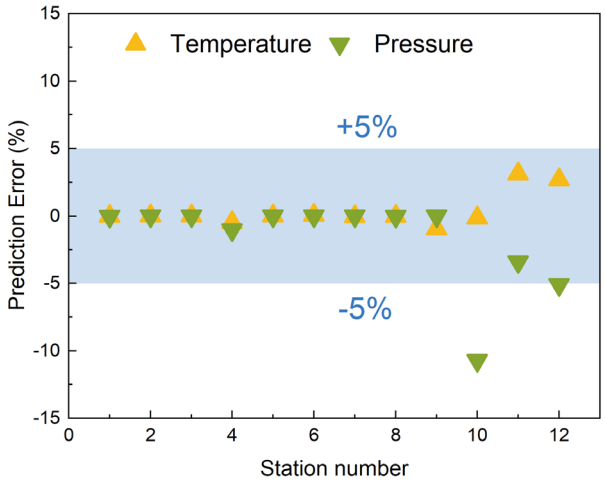


Figure 3: Prediction error distributions across all evaluated data points.

Figure 4 displays the variation trends in pressure and temperature across engine components from both models. The largest temperature and pressure deviations are 23.2 K and 54.8 kPa, respectively—both within acceptable ranges. Notably, larger discrepancies occur in the turbine section, which is attributed to the reference model's omission of exhaust gas property variations and $k_g$ shifts with temperature and pressure. In contrast, the present model dynamically updates working fluid properties based on local thermodynamic conditions. In general, the small deviations validate the accuracy and robustness of the proposed modeling approach.

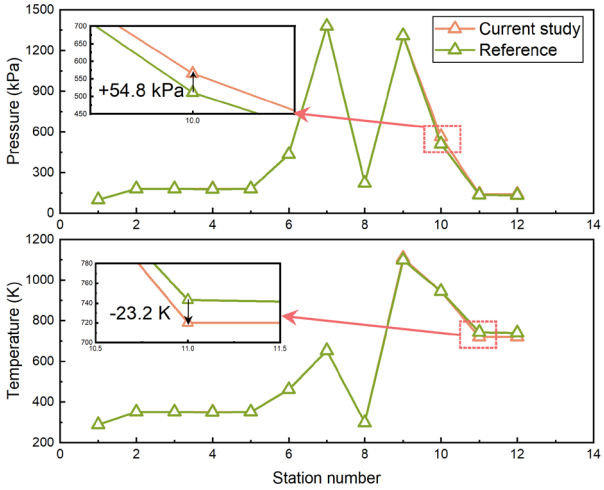


Figure 4: Variation trends in pressure and temperature across engine components from both models.

## 4. Results and discussion

This study presents a comprehensive comparison of the proposed aviation gas turbine engine operating on liquid hydrogen and kerosene, under consistent baseline assumptions. The thermodynamic performance indicators for hydrogen and kerosene fuels, as listed in Table 3 [17], are evaluated. Thermal performance, economic indicators, and thrust characteristics are compared for both fuels across various flight conditions.

Table 3: Thermodynamic indicators related to aviation engines.

| Thermodynamic indicators | Definitions | Eqs. |
|---|---|---|
| Thrust, $F$ | The force generated by the engine to propel the aircraft forward. | $F = m_{11}V_{\mathrm{EDN}} + m_{1.2}V_{\mathrm{FDN}} - m_1V_1$ |
| Specific thrust, $F_s$ | Thrust produced per unit mass flow rate of air through the engine; indicates the engine's propulsion efficiency. | $F_s = F / m_1$ |
| Thermal efficiency, $\eta_{th}$ | The ratio of the net work output to the thermal energy input from fuel; reflects how effectively the engine converts fuel energy into mechanical energy. | $\eta_{\mathrm{th}} = \dfrac{\left(m_{11}V_{\mathrm{EDN}}^2 + m_{1.2}V_{\mathrm{FDN}}^2 - m_1V_1^2\right)/2}{m_6 LHV \times 1000}$ |
| Propulsive efficiency, $\eta_P$ | The ratio of the thrust power to the rate at which kinetic energy is imparted to the exhaust jet and the aircraft; reflects how effectively the engine converts mechanical energy into thrust to propel the aircraft. | $\eta_{\mathrm{p}} = \dfrac{\left(m_{11}V_{\mathrm{EDN}} + m_{1.2}V_{\mathrm{FDN}}\right)V_1 - m_1V_1^2}{\left(m_{11}V_{\mathrm{EDN}}^2 + m_{1.2}V_{\mathrm{FDN}}^2 - m_1V_1^2\right)/2}$ |
| Overall efficiency, $\eta_0$ | The ratio of the useful propulsive power output to the thermal energy input from fuel | $\eta_0 = \eta_{\mathrm{th}}\eta_{\mathrm{p}}$ |
| Specific fuel consumption, $SFC$ | The fuel mass flow rate required to produce a unit of thrust; an indicator of engine fuel efficiency. | $SFC = \dfrac{3600m_6}{F}$ |
| Fuel cost rate, $FCR$ | The monetary cost of fuel consumed per unit time. $H_2$ selling price is 4.94 \$/kg [27]. | $FCR = 4.94m_6$ |
| Specific fuel cost rate, $SFCR$ | The ratio of fuel cost rate to engine thrust; quantifies the economic cost of fuel per unit of thrust, typically expressed in \$/(kN·s). | $SFCR = \dfrac{FCR}{F}$ |

The properties of the fuels subject to study are presented in Table 4 [17]. In calculating the heat input to the cycle, the $LHV$s of kerosene and hydrogen are taken as 43254 kJ/kg and 119450 kJ/kg, respectively. The energy input to the cycle, or the heat transfer rate $Q_{CC}$, is calculated as 147165.3 kW for each fuel, with corresponding fuel mass flow rates of 3.44 kg/s for kerosene and 1.24 kg/s for hydrogen.

Table 4: Benchmarking of the fuel's properties subject to analysis.

| Fuel | LHV (kg/kg) | Fuel mass flow rate (kg/s) | Energy input (kW) |
|---|---|---|---|
| Hydrogen | 119450 | 1.24 | 141765.3 |
| Kerosene | 43254 | 3.44 | 141765.3 |

### 4.1 Comparison of temperature variations across components under sea-level takeoff conditions

Figure 5 illustrates the temperature variations across components when the proposed engine operates with two different fuels under $Ma = 0$ and $H = 0$ m. The blue-shaded area indicates the region occupied by the ICHE system, while the orange-shaded area represents the region of the recuperator. Detailed temperature data are provided in Table 5. It can be observed that the thermodynamic performance differences between the two fuels originate in the ICHE system. Owing to the higher heat sink capacity of liquid hydrogen compared to kerosene, as well as its significantly lower storage temperature and the latent heat involved during vaporization, the ICHE system exhibits superior heat transfer performance when operating with liquid hydrogen. Consequently, lower HPC inlet temperatures and turbine cooling air temperatures are achieved. Specifically, compared to kerosene, the use of hydrogen fuel results in a 43.2 K reduction in HPC inlet temperature and a 179.5 K reduction in turbine cooling air temperature, thereby decreasing the workload on the HPC rotor and enabling more effective turbine cooling. Moreover, the use of hydrogen fuel leads to a reduced combustor inlet air temperature $T_{5.3}$. Specifically, $T_{5.3}$ is 738.70 K for hydrogen fuel, compared to 815.56 K for kerosene. According to Eq. (8), this further results in a lower turbine inlet temperature $T_7$ under equivalent heat release—196.9 K lower than that of kerosene—thereby reducing the thermal load on the turbine. For the recuperator, since it is located at the outlet of the LPT, the exhaust gas temperature passing through it is lower when hydrogen fuel is used. However, this does not result in significant performance gains for the engine. The comparative results of the engine's thermodynamic performance indicators will be presented in the following section.

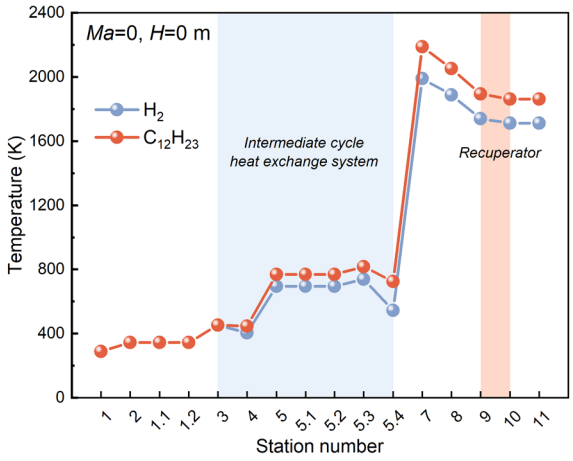


Figure 5: Temperature variation of the flow through the components in the case of the engine operating separately with both fuels when $Ma = 0$ and $H = 0$ m.

Table 5: Temperatures at different stations in the case of the engine operating separately with both fuels when $Ma = 0$ and $H = 0$ m.

| Station | Hydrogen $T$ (K) | Kerosene $T$ (K) | Station | Hydrogen $T$ (K) | Kerosene $T$ (K) |
|---|---|---|---|---|---|
| 1 | 288.15 | 288.15 | 5.3 | 738.70 | 815.56 |
| 2 | 343.05 | 343.05 | 5.4 | 544.91 | 724.38 |
| 1.1 | 343.05 | 343.05 | 7 | 1990.47 | 2187.36 |
| 1.2 | 343.05 | 343.05 | 8 | 1888.12 | 2052.47 |
| 3 | 451.34 | 451.34 | 9 | 1739.82 | 1894.81 |
| 4 | 403.70 | 446.87 | 10 | 1711.43 | 1862.38 |
| 5 | 693.14 | 767.26 | 11 | 1711.43 | 1862.38 |
| 5.1 | 693.14 | 767.26 | 12 | 303.02 | 489.84 |
| 5.2 | 693.14 | 767.26 | 13 | 27.37 | 338.10 |

### 4.2 Comparison of thermodynamic characteristics under different flight conditions

This section compares the thermodynamic characteristics of the proposed engine under three flight conditions (as shown in Table 6) when using hydrogen fuel versus aviation kerosene, with a focus on the heat transfer performance of the four HEXs and the various thermodynamic indicators listed in Table 3.

Table 6: Flight conditions this work studied.

| | Case A | Case B | Case C |
|---|---|---|---|
| *Ma* | 0 | 0.85 | 1.1 |
| *H* | 0 m | 10000 m | 12000 m |

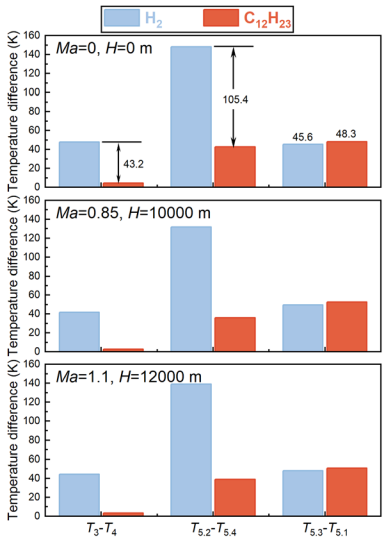


Figure 6: Temperature difference on the air side of the HEXs under different flight conditions.

Figure 6 presents the variations in air-side inlet and outlet temperatures of different HEXs within the engine under various flight conditions, where $T_3-T_4$ corresponds to HEX-1, $T_{5.2}-T_{5.4}$ to HEX-2, and $T_{5.3}-T_{5.1}$ to HEX-4. It can be observed that the air-side temperature differences of HEX-1 and HEX-2 are significantly larger when hydrogen fuel is used compared to kerosene. Under the sea-level takeoff condition, $T_3-T_4$ increases by 43.2 K and $T_{5.2}-T_{5.4}$ increases by 105.4 K. In contrast, the air-side temperature difference in the recuperator shows minimal variation between the two fuels, remaining within 1 K. This indicates that the use of hydrogen fuel significantly enhances the effectiveness of intercooling and compressor bleed air cooling, attributable to the low-temperature characteristics of hydrogen and the heat sink transfer enabled by the ICHE system. Since the ICHE system is not directly connected to the recuperator, the choice of fuel has only a minor indirect impact on it.

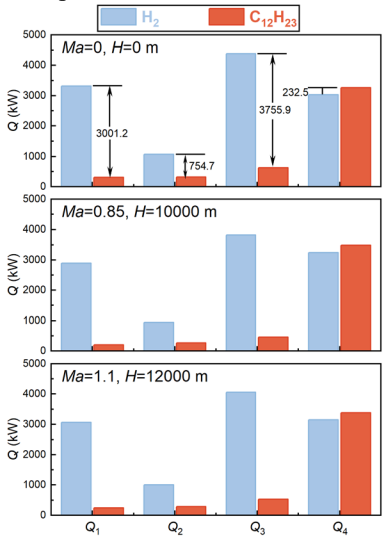


Figure 7: Heat transfer rates of various HEXs under different flight conditions.

The comparison of heat transfer rates for each HEX within the engine is shown in Fig.7. Across various flight conditions, heat transfer rates in all ICHE system HEXs are significantly higher with hydrogen fuel, whereas the recuperator exhibits negligible variation. For instance, under sea-level takeoff conditions, the intercooler $Q_1$, CCA cooler $Q_2$, and fuel preheater $Q_3$ with hydrogen are 10.63, 3.37, and 6.96 times higher than those with kerosene, respectively. The greater difference in $Q_1$ is primarily due to the larger helium flow distribution ratio ($\phi$) across branches in the simulation, where $\phi$ = 0.8. This indicates that a larger helium mass flow passes through HEX-1, resulting in a higher cooling capacity for HEX-1. These pronounced differences underscore the advantages of applying an ICHE system in hydrogen-fueled turbofan engines, enabling deep cascade energy utilization. This enhancement primarily results from liquid hydrogen's inherently low temperature and high heat sink capacity. Although the benefits of kerosene are less pronounced, 630.2 kW of heat is still transferred from high-pressure air to the fuel, reducing compressor airflow temperature and preheating the kerosene to promote combustion. Figure 8 demonstrates the differences in turbine inlet temperature $T_7$ and recuperator inlet temperature $T_9$ under various flight conditions when using different fuels. It can be seen that, under the same combustion heat release, the higher compressor outlet air temperature associated with kerosene leads to higher $T_7$ and $T_9$. Under the sea-level takeoff condition, $T_7$ with kerosene is 196.9 K higher than that with hydrogen, and $T_9$ is 155.0 K higher, subjecting both the turbine and recuperator to greater thermal loads and imposing stricter requirements on material properties and service life. However, the increase in $T_9$ also enlarges the temperature difference across the recuperator, leading to a higher $Q_4$ compared to hydrogen. In other words, kerosene enables more recovery of turbine exhaust heat than hydrogen, although the difference is not particularly significant.

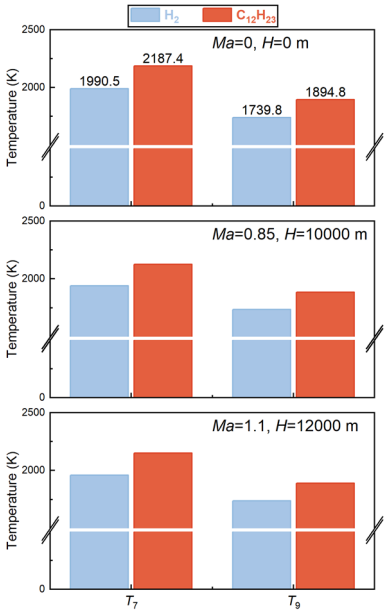


Figure 8: Comparison of turbine inlet temperature $T_7$ and recuperator inlet temperature $T_9$ between hydrogen and kerosene under different flight conditions.

Table 7 presents a comparison of the thermodynamic performance indicators of the proposed engine under three flight conditions. It can be seen that the engine equipped with the ICHE system and recuperator exhibits outstanding performance. Under high-altitude supersonic flight conditions (Case C), the engine achieves a thrust of 98.95 kN and a specific thrust of 659.69 (N·s)/kg when using hydrogen fuel. Notably, the thermal efficiency reaches 0.60 and the propulsive efficiency reaches 0.36, both of which represent exceptionally high levels for a turbofan engine. In addition, it is observed that the engine's thrust, specific thrust, thermal efficiency, propulsive efficiency, and overall efficiency show no significant differences between hydrogen and kerosene fuels—the performance is nearly identical. The primary differences between the two fuels lie in the specific fuel consumption (*SFC*) and the specific fuel cost rate (*SFCR*). Hydrogen fuel use markedly reduces the engine's SFC. Across multiple flight conditions, hydrogen *SFC* is approximately 0.33–0.40 times that of kerosene, indicating lower fuel consumption and higher fuel efficiency. However, due to the high cost of liquid hydrogen, the fuel cost rate (*FCR*) reaches 6.13 $/s for hydrogen versus 1.58 $/s for kerosene, resulting in a *SFCR* approximately 3–5 times greater—thus implying higher operational costs. Overall, although hydrogen fuel increases operating costs, it markedly reduces the engine's *SFC*. Efficient utilization of liquid hydrogen's cryogenic heat sink and ICHE–recuperator integration substantially enhances thermal efficiency. Furthermore, the absence of carbon emissions strongly supports sustainable development in the aviation sector.

Table 7: Comparison of thermodynamic performance indicators under different flight conditions.

| Thermodynamic indicators | Case A | | Case B | | Case C | |
|---|---|---|---|---|---|---|
| | Hydrogen | Kerosene | Hydrogen | Kerosene | Hydrogen | Kerosene |
| $F$ [kN] | 125.24 | 126.06 | 101.89 | 101.67 | 98.95 | 98.59 |
| $F_s$ [(N·s)/kg] | 834.92 | 840.39 | 679.24 | 677.77 | 659.69 | 657.29 |
| $\eta_{th}$ | 0.50 | 0.49 | 0.57 | 0.55 | 0.60 | 0.57 |
| $\eta_p$ | 0.00 | 0.00 | 0.31 | 0.32 | 0.36 | 0.37 |
| $\eta_0$ | 0.00 | 0.00 | 0.18 | 0.17 | 0.22 | 0.22 |
| $SFC$ [kg/(N·h)] | 0.04 | 0.10 | 0.04 | 0.12 | 0.05 | 0.13 |
| $FCR$ [$/s] | 6.13 | 1.58 | 6.13 | 1.58 | 6.13 | 1.58 |
| $SFCR$ [$/(kN·s)] | 0.05 | 0.01 | 0.06 | 0.02 | 0.06 | 0.02 |

## 5. Conclusion

This study develops and validates a thermodynamic model for a hydrogen-fueled turbofan engine featuring an intermediate cycle heat exchange system and a recuperator. Comparative analysis shows that, relative to kerosene, hydrogen significantly improves thermal management—reducing the high-pressure compressor inlet temperature by 43.2 K, turbine cooling air temperature by 179.5 K, and turbine inlet temperature by 196.9 K. The heat transfer rates of the intercooler, CCA cooler, and fuel preheater under hydrogen operation are 10.63, 3.37, and 6.96 times those under kerosene, respectively. While hydrogen increases the fuel cost rate (6.13 $/s vs. 1.58 $/s), it reduces the specific fuel consumption to approximately 0.33–0.40 times that of kerosene. At high-altitude conditions ($Ma$ = 1.1, $H$ = 12000 m), the engine reaches a thermal efficiency of 0.60 and a propulsive efficiency of 0.36, delivering 98.95 kN of thrust. These results highlight hydrogen's excellent energy utilization and decarbonization potential, confirming its viability for future sustainable aviation propulsion.

## Acknowledgment

The authors appreciate the supports from the Beijing Nova Program (No. 20240484560), Beijing Municipal Science & Technology Commission, Administrative Commission of Zhongguancun Science Park (No. Z241100007424005), and the Academic Excellence Foundation of BUAA for PhD Students.

## References

[1] Oğur E, Koç A, Köse Ö, Yağlı H, Koç Y. 2025. Energy, exergy, exergoeconomic, exergy sustainability and exergoenvironmental analyses (5E) of a turbofan engine: A comparative study of hydrogen and kerosene fuels. *Fuel*. 381.

[2] GG F, I dLe, R S. Environmental trends in aviation to 2050 background. 2023.

[3] Capitao Patrao A, Jonsson I, Xisto C, Lundbladh A, Lejon M, Grönstedt T. 2024. The heat transfer potential of compressor vanes on a hydrogen fueled turbofan engine. *Applied Thermal Engineering*. 236.

[4] Berg F, Palmer J, Miller P, Dodds G. 2017. HTS System and Component Targets for a Distributed Aircraft Propulsion System. *IEEE Transactions on Applied Superconductivity*. 27: 1-7.

[5] Abedi H, Xisto C, Jonsson I, Grönstedt T, Rolt A. 2022. Preliminary Analysis of Compression System Integrated Heat Management Concepts Using LH2-Based Parametric Gas Turbine Model. *Aerospace-Basel*. 9.

[6] Tiwari S, Pekris MJ, Doherty JJ. 2024. A review of liquid hydrogen aircraft and propulsion technologies. *Int J Hydrogen Energ*. 57: 1174-96.

[7] Wang X, He A, Hu Z. 2023. Transient Modeling and Performance Analysis of Hydrogen-Fueled Aero Engines. *Processes*. 11.

[8] Norris G. 2022. Pratt Outlines Hydrogen Steam-Injection Engine Concept. *Aviation Week& Space Technology, April*. 19.

[9] Webber H, Llambrich J, Davoudi H. 2022. FlyZero: Thermal management roadmap report. *Aerospace Technology Institute*.

[10] Patrao AC, Jonsson I, Xisto C, Lundbladh A, Grönstedt T. 2024. Compact heat exchangers for hydrogen-fueled aero engine intercooling and recuperation. *Applied Thermal Engineering*. 243.

[11] Fu Y, Liu W, Wang J, Zhang L, Wen J, Wu H, et al. 2024. Experimental investigation on heat transfer enhancement of supercritical pressure aviation kerosene in tubular laminar flow by vibration. *Applied Thermal Engineering*. 257.
[12] Fu Y, Liu W, Qi H, Chen Q, Wen J, Xu G. 2024. Heat transfer area optimization of intermediate heat-exchange cycle system for aero engines. *International Journal of Heat and Mass Transfer*. 220.
[13] Liu W, Xu G, Zhi H, Wang R, Li M, Fu Y. 2024. Experimental evaluation of hydrothermal performance in airfoil-fin PCHE with supercritical pressure hydrocarbon fuel. *International Communications in Heat and Mass Transfer*. 159.
[14] Liu W, Xu G, Gu X, Yao J, Li M, Lei M, et al. 2025. Experimental analysis and thermodynamic modeling for multilevel heat exchange system with multifluid in aero engines. *Energy*. 315.
[15] Liu W, Xu G, Gang X, Qi H, Li M, Wen J, et al. 2024. Theoretical modeling, experimental validation, and thermodynamic analysis on intermediate heat-exchange cycle system. *International Communications in Heat and Mass Transfer*. 156.
[16] Ang EYM, Ng PS, Soh CB, Wang PC. 2022. Multi-stage thermoelectric coolers for cooling wearables. *Thermal Science and Engineering Progress*. 36.
[17] Balli O, Ozbek E, Ekici S, Midilli A, Hikmet Karakoc T. 2021. Thermodynamic comparison of TF33 turbofan engine fueled by hydrogen in benchmark with kerosene. *Fuel*. 306.
[18] Oğur E, Koç A, Yağlı H, Koç Y, Köse Ö. 2024. Thermodynamic, economic, and environmental analysis of a hydrogen-powered turbofan engine at varying altitudes. *Int J Hydrogen Energ*. 55: 1203-16.
[19] Derakhshandeh P, Ahmadi A, Dashti R. 2021. Simulation and technical-economic-environmental optimization of the General Electric GE90 hydrogen turbofan engine. *Int J Hydrogen Energ*. 46: 3303-18.
[20] Akdeniz HY, Balli O. 2022. Impact of different fuel usages on thermodynamic performances of a high bypass turbofan engine used in commercial aircraft. *Energy*. 238.
[21] Colera M, Soria Á, Ballester J. 2019. A numerical scheme for the thermodynamic analysis of gas turbines. *Applied Thermal Engineering*. 147: 521-36.
[22] Chen Q, Hao J, Zhao T. 2017. An alternative energy flow model for analysis and optimization of heat transfer systems. *International Journal of Heat and Mass Transfer*. 108: 712-20.
[23] Zhao T, Chen X, He K-L, Chen Q. 2021. A standardized modeling strategy for heat current method-based analysis and simulation of thermal systems. *Energy*. 217.
[24] Bell IH, Wronski J, Quoilin S, Lemort V. 2014. Pure and pseudo-pure fluid thermophysical property evaluation and the open-source thermophysical property library CoolProp. *Ind Eng Chem Res*. 53: 2498-508.
[25] Xu W, Li Q, Huang M. 2015. Design and analysis of liquid hydrogen storage tank for high-altitude long-endurance remotely-operated aircraft. *Int J Hydrogen Energ*. 40: 16578-86.
[26] Liu W, Xu G, Fu Y, Wen J, Zhang N. 2023. Numerical investigation on forced, natural, and mixed convective heat transfer of n-decane in laminar flow at supercritical pressures. *International Journal of Heat and Mass Transfer*. 209.
[27] Razi F, Dincer I, Gabriel K. 2020. A specific exergy costing assessment of the integrated copper-chlorine cycle for hydrogen production. *Int J Hydrogen Energ*. 45: 31425-39.